Geometrical properties of three-dimensional crossed nanowire networks

Tristan da Câmara Santa Clara Gomes,[1] Nicolas Marchal,[1] Anatole Moureaux,[1] Simon de Wergifosse,[1] Chloé Chopin,[1] Luc Piraux,[1] Joaquín de la Torre Medina,[2] and Flavio Abreu Araujo[1,*]

[1]*Institute of Condensed Matter and Nanosciences, Université catholique de Louvain, Place Croix du Sud 1, 1348 Louvain-la-Neuve, Belgium*
[2]*Instituto de Investigaciones en Materiales–Unidad Morelia, Universidad Nacional Autónoma de México, Morelia 58000, Mexico*

Three-dimensional interconnected nanowire networks have recently attracted notable attention for the fabrication of new devices for energy harvesting/storage, sensing, catalysis, magnetic and spintronic applications, and for the design of new hardware neuromorphic computing architectures. However, the complex branching of these nanowire networks makes it challenging to investigate these 3D nanostructured systems theoretically. Here, we present a theoretical description and simulations of the geometric properties of these 3D interconnected nanowire networks with selected characteristics. Our analysis reveals that the nanowire segment length between two crossing zones follows an exponential distribution. This suggests that shorter nanowire segments have a more pronounced influence on the nanowire network properties compared to their longer counterparts. Moreover, our observations reveal a homogeneous distribution in the smallest distance between the cores of two crossing nanowires. The results are highly reproducible and unaffected by changes in the nanowire network characteristics. The density of crossing zones and interconnected nanowire segments is found to vary as the square of the nanowire density multiplied by their diameter, further multiplied by a factor dependent on the packing factor. Finally, densities of interconnected segments up to 10^{13} cm^{-2} can be achieved for 22-μm-thick nanowire networks with high packing factors. This has important implications for neuromorphic computing applications, suggesting that the realization of 10^{14} interconnections, which corresponds to the approximate number of synaptic connections in the human brain, is achievable with a nanowire network of about 10 cm^2.

I. INTRODUCTION

Three-dimensional (3D) networks made of interconnected nanowires (NWs) and nanotubes (NTs) have been developed in the past decades, raising interest due to their unique architecture with a high degree of NW interconnectivity, mechanical, and functional properties [1–5]. Notably, the system has potential applications in a wide range of fields such as in energy harvesting/storage systems [6–8], electronic sensing devices and actuators [9–11], catalysts [1], electrochromic elements [12], solar cells [13], biosensors [14], bioanalytical devices [15,16], photonic devices [2], thermal regulators [17], magnetic memory [18], spintronics[5,19–21], thermoelectric devices [22–27], spin caloritronic devices [28–32], and unconventional computing [33–35]. The NW branching structure offers a good mechanical stability to the networks, which have been found to be self-supported [4,19,20]. Moreover, the NW interconnections allow one to easily measure electrical and thermoelectrical properties of these nanostructures. However, despite the interest generated by the architecture,

theoretical and simulation studies are still lacking to provide a better understanding of 3D crossed NW networks. This is due to the complexity of the nanostructure. Here, we propose theoretical and simulation studies of the geometrical properties of 3D interconnected NW networks with various selected characteristics.

Three-dimensional NW networks are a unique nanoarchitecture made of interconnected NWs to form a mechanically stable and self-supported film. Electrodeposition into well-designed track-etched polymer templates has been proved to be a suitable and low-cost synthesis technique to fabricate 3D nanowire networks with very different geometrical characteristics [1,3], such as mean NW diameter D, the angle with the network film normal θ, the packing factor P, and the film thickness h. Here, we propose the study of NW networks film with characteristics corresponding to recent studies by Piraux *et al.* [4]. In this system, NWs are grown into well-defined templates with crossed cylindrical nanochannels, which are created by exposing a polycarbonate film to four irradiation steps with different incident angles. Considering the z direction as the normal direction of the film, and the x and y directions as two orthogonal in-plane directions of the film, as illustrated in Fig. 1(a), the four resulting nanopore families make angles of $-\theta$ and $+\theta$ with respect to the z direction in the plane x-z and y-z, with θ encompassed between 20° and 25°. We will consider different high-porosity systems with diameters of $D \approx 20$ nm, 40 nm, 105 nm, and 230 nm and respective ion impact surface densities n
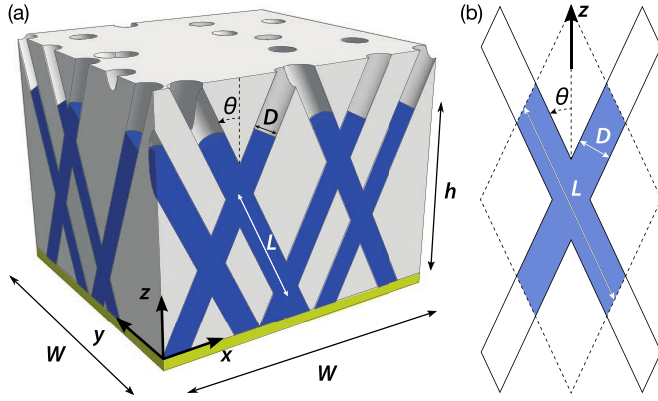
*flavio.abreuaraujo@uclouvain.be

FIG. 1. (a) Schematic representation of the simulated volume of 3D nanowire network and its dimensions, W being the side of the network film surface considered and h the network film thickness. The nanowires of diameter D make an angle θ with the surface normal of the network film, which is the z direction. The x and y directions refer to two perpendicular directions in the plane of the network film surface. The interdistance between centers of nanowire crossing zones is noted L. (b) Unit cell of two crossed nanowires for an interdistance L between centers of nanowire crossing zones.

of 4.8×10^{10} cm^{-2}, 1.2×10^{10} cm^{-2}, 2.4×10^{9} cm^{-2}, and 5.0×10^{8} cm^{-2}. The porosity of the template can be estimated as $P = n\pi D^2/4$, which yields respectively $P \approx 15\%$, 15%, 21%, and 21% for the high-porosity systems studied. Additionally, we will consider two low-porosity systems with $D \approx$ 40 nm and 80 nm, and $n = 6 \times 10^8$ cm^{-2}, giving respectively $P \approx 0.8\%$ and 3%. Note that the porosity of the template is assumed to be identical to the NW network packing factor, indicating that the entire template is considered as filled with NWs.

The complex nanoarchitecture is simulated in a specified volume $V = W^2 h$ of the interconnected NW structure, where W is the side of a square on the plan (x, y) of the film surface and h is the film thickness along the z direction. This specified volume directly depends on the number of surface irradiation impacts $N = 4N_f$ selected, where N_f is the number of surface impacts for each of the four families of nanopores. These four families are defined as follows:

(1) Family 1: Making an angle of $+\theta$ with the z direction in the plane x-z.

(2) Family 2: Making an angle of $-\theta$ with the z direction in the plane x-z.

(3) Family 3: Making an angle of $+\theta$ with the z direction in the plane y-z.

(4) Family 4: Making an angle of $-\theta$ with the z direction in the plane y-z.

The studied volume is illustrated in Fig. 1(a) with the different parameters. In addition, Fig. 1(b) shows the NW crossing unit cell, which depends on the length L between the centers of two successive NW interconnections. Using the surface density of impact n, the length W is obtained as $W = \sqrt{N/n}$, while the thickness is selected by assuming that if a NW begins at one edge of the surface, its end is located on the opposite edge, which gives $h = W/\tan\theta$. Taking the thickness h as fixed by the system, it yields a number of surface irradia-

tion impacts $N = n(h\tan\theta)^2$, which is rounded to the closest multiple of four to account for the four identical irradiations for each of the four families. The center of the irradiation impact (x_0, y_0) of each nanopore from the four families on the surface $z = 0$ is randomly chosen. Figure 2 shows the bottom surface $(z = 0)$ for $D = 40$ nm, $n = 1.2 \times 10^{10}$ cm^{-2}, and $h = 22$ μm, where each of the four nanopore families is indicated in a different color. The NW segments are simulated by cylinders of diameter D along straight lines (referred as NW axes) with orientation vector $(a\sin\theta, b\sin\theta, \cos\theta)$, where a and b are constants that depend on their family, as provided in the inset of Fig. 2. Moreover, NWs engendered by impacts from outside the considered surface can also induce crossings inside the considered volume. Therefore, NWs from each family are also created from N additional impacts randomly chosen outside the surface as shown in Fig. 2. The NWs originating from inside the surface of the volume of interest are noted as "in," while the NWs originating from outside the surface of the volume of interest are noted as "out." This virtual NW network has been used for all the following characterizations.

II. NANOWIRE SEGMENT LENGTH DISTRIBUTION

In this section, we present the derivation of the statistical distribution of the interdistance between two successive crossing points, noted L, obtained through simulations. A crossing point is defined as the center of the interconnection volume between two NWs. Understanding the distribution of L is essential for simulating the structure of crossed NWs, as it plays a crucial role in defining the unit cell of the crossed NW configuration, which is illustrated in Fig. 1(b). In addition, we derive the shortest distance between the axes of two NWs, denoted as d. This distance varies from zero for NWs with axes intersecting, to $\pm D/2$ for NWs that only touch each other. Furthermore, we investigate the densities of interconnections and NW segments, as well as the proportion of interconnections involving two, three, or more NWs. For this approach, the crossing conditions are separated into three main categories:

(i) Crossing between two NWs generated from impacts at the bottom surface of the considered volume.

(ii) Crossing between a NW generated from impacts at the bottom surface of the considered volume and a NW generated from impacts outside of the bottom surface of the considered volume.

(iii) Crossing between two NWs generated from impacts outside the bottom surface of the considered volume.

Note that we exclude the possibility of interconnection between two nanowires belonging to the same family, as the angle is considered as fixed. Therefore, the length between two crossing points is expected to be slightly overestimated.

We analyze each pair of simulated NW axes, represented by orientation vectors $(a_1\sin\theta, b_1\sin\theta, \cos\theta)$ and $(a_2\sin\theta, b_2\sin\theta, \cos\theta)$ for the first and second NWs considered, respectively, along with their respective irradiation impact centers $(x_0, y_0)_1$ and $(x_0, y_0)_2$. We always designate the first NW as the one with the smaller family index. The shortest distance $|d|$ between two NWs' axes is computed using the
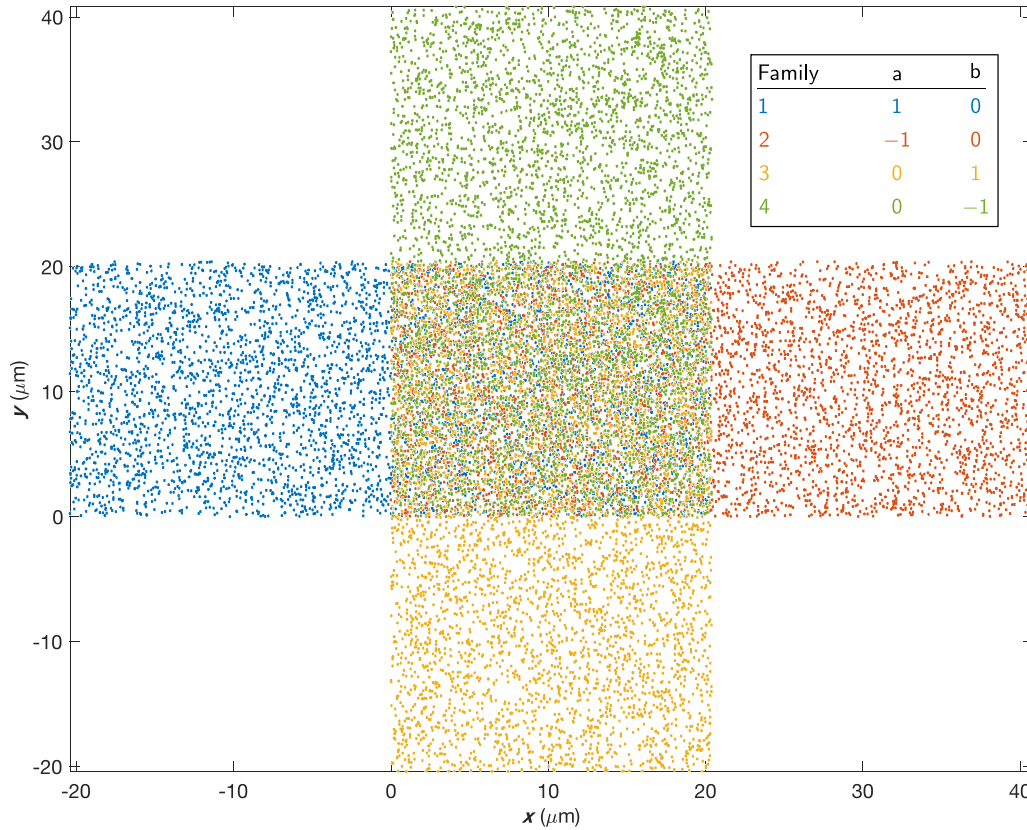
FIG. 2. Schematic representation of the nanowire network film surface ($z = 0$) along with the irradiation impacts randomly generated for the characterization of the geometry of the interconnected structure. Each dot represents one impact, the four families corresponding to the four different colours. The inset provides the values of the constants a and b needed for the orientation vectors for each of the four nanowire families.

formula

$$d = \left| \frac{(b_1 - b_2)\Delta x - (a_1 - a_2)\Delta y}{\sqrt{K}} \right|, \qquad (1)$$

where $K = (a_1 - a_2)^2 + (b_1 - b_2)^2 + (a_1^2 b_2^2 + a_2^2 b_1^2)\tan^2\theta$ and the difference between the center of impacts $(\Delta x, \Delta y)$ is defined as $(x_0, y_0)_1 - (x_0, y_0)_2$. A crossing point is considered only if this distance $|d|$ is smaller that the diameter D and is located within the total volume ($W \times W \times h$) considered in our simulations. The computed values of K and $|d|$ for each pair of families are reported in Table S1 in Supplemental Material [36] Sec. S1, together with the detailed conditions for crossing (see Table S2 [36]).

The position of the crossing point on the two NW axes, which are noted P_1 and P_2, are computed as

$$P_1 = \frac{-\Delta x(a_1 - a_2 + b_2 K_1) - \Delta y(b_1 - b_2 + a_2 K_2)}{K \sin\theta} \qquad (2)$$

and

$$P_2 = \frac{-\Delta x(a_1 - a_2 - b_1 K_2) - \Delta y(b_1 - b_2 - a_1 K_1)}{K \sin\theta}, \qquad (3)$$

with $K_1 = a_1 b_2 \tan^2\theta$ and $K_2 = a_2 b_1 \tan^2\theta$. After computing the crossing positions P_i for each NW, the interdistances L between two crossing points are obtained by computing the distances between successive crossing positions P_i.

First, a NW network with $D = 40$ nm, $\theta = 22.5°$, $n = 1.2 \times 10^{10}$ cm^{-2}, $W = 9.1$ μm, $h = 22$ μm, which corresponds to $N = 9964$ NWs, is simulated. A set of 1000 simulations of the system generates a mean value of about 538 000 crossing points (with a standard deviation of about 0.2%), which corresponds to about 294 crossing points per μm^3. The distribution of the interdistance between two centers of successive NW interconnections L is shown in Fig. 3(a) for this network. It shows an exponential distribution with a mean value of $\lambda = 216$ nm (this value is identical to the standard deviation of the exponential distribution). This value fluctuates by approximately 0.3% across a set of 1000 simulations. As seen in Fig. 3(a), the theoretical exponential law $1/\lambda \exp(l/\lambda)$ corresponds well to the simulated data. The largest interdistance between two crossing points is slightly larger than 3 μm. In addition, we observe that 99% of the segments between two crossing points are below 1 μm. Furthermore, we find that 60% of the crossing points involve perpendicular families. In addition, the inset of Fig. 3(a) shows the distribution of the shortest distance d between two crossing NWs' axes. As seen, it displays a homogeneous distribution between -40 nm and 40 nm, which corresponds to the value of the diameter D as expected as two NWs can only cross if the shortest distance between them is less than the diameter. These simulations are repeated several times with very similar results at each run (the mean value and standard deviation of λ for 100 runs with these parameters are 216.2 nm and 0.4 nm). Figure 3(b) shows
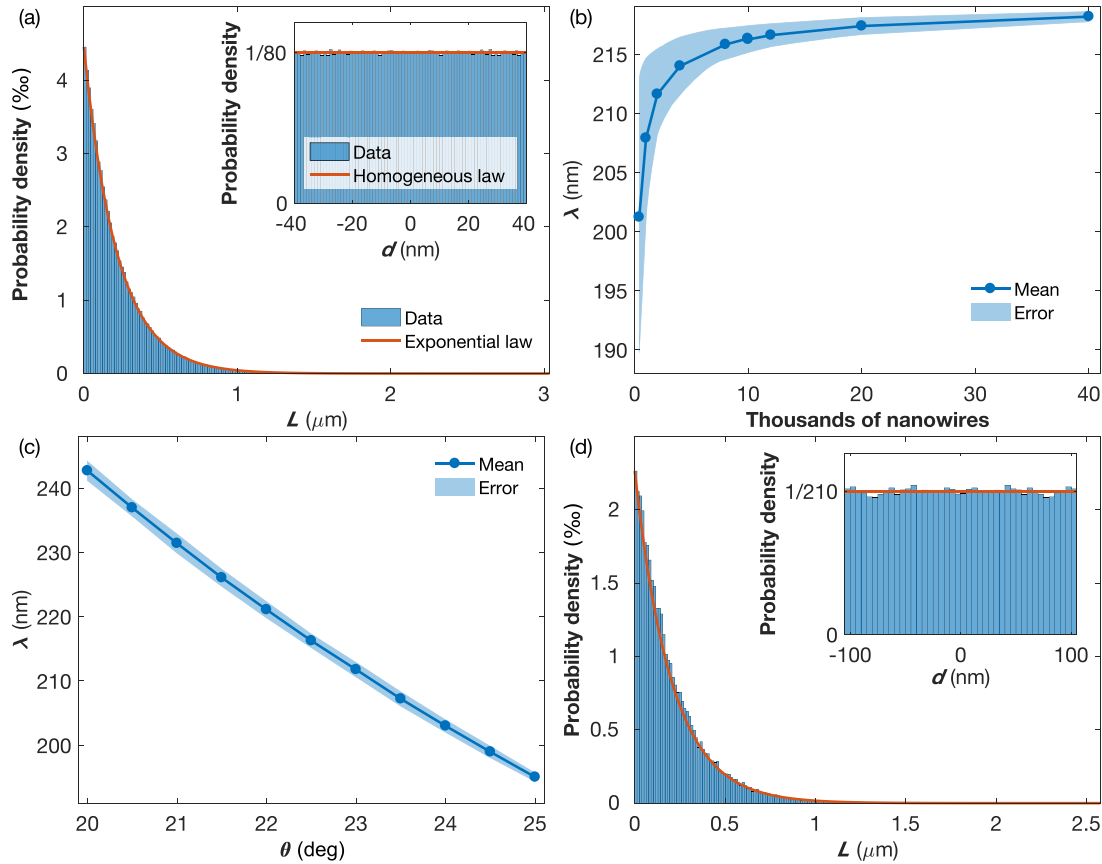
FIG. 3. (a) Probability density for the length between two successive crossing points, showing the simulated data (in blue) for $D = 40$ nm, $\theta = 22.5°$, $n = 1.2 \times 10^{10}$ cm^{-2}, and $h = 22$ μm, and an exponential law $1/\lambda \exp(l/\lambda)$ (in red) with λ taken as the mean length between two successive crossing points. The inset shows the corresponding probability density for the shortest distance between two crossing nanowires axes with the same parameter, including the simulated data (in blue) and a homogeneous law $1/(2D)$. (b) Mean length between two successive crossing points as a function of the number of simulated nanowires (in thousands) taken as the mean value over 100 simulations for a nanowire network with 40 nm in diameter and about 15% in packing factor. (c) Mean length between two successive crossing points as a function of the angle θ taken as the mean value over 100 simulations for a nanowire network with 40 nm in diameter and about 15% in packing factor. The blue areas in (b) and (c) show the error taken as 3 times the standard deviation over 100 runs. (d) Probability density for the length between two successive crossing points, showing the simulated data (in blue) for $D = 105$ nm, $\theta = 22.5°$, $n = 2.4 \times 10^9$ cm^{-2}, and $h = 22$ μm, and an exponential law $1/\lambda \exp(l/\lambda)$ (in red) with λ taken as the mean length between two successive crossing points. The inset shows the corresponding probability density for the shortest distance between two crossing nanowire axes with the same parameters, including the simulated data (in blue) and a homogeneous law $1/(2D)$.

the mean value of λ as a function of the number N of simulated irradiation impacts on the surface of the simulated volume while keeping the same surface density of impacts n, obtained on 100 runs for each value of N. The blue area shows the error taken as three times the standard deviation for these 100 runs (gathering 99.7% of the variation). As seen, the mean value converges when the value of N is increased while the error decreases as expected from the law of large numbers.

In the real system, the angle θ varies between 20° and 25°, which is expected to modify the mean length between two successive crossing points. Indeed, a change in θ is expected to modify the probability of crossing NWs from other families, as well as to induce additional crossings between NWs of the same family. However, this largely complicates the simulation. Instead of randomly affecting an angle θ between 20° and 25° to each NW, the value of θ is taken as the same value for all NWs and varied from 20° to 25°, while the packing factor of the NW networks is maintained by adapting

the studied volume dimensions. This gave a first step toward understanding the effect of θ on the NW network properties. Figure 3(c) provides the mean value of λ for 100 runs as a function of θ, while the other parameters are kept unchanged ($D = 40$ nm and $n = 1.2 \times 10^{10}$ cm^{-2}). The blue area in Fig. 3(c) provides the error taken as three times the standard deviation. As expected, the larger the value of θ the lower the mean distance between two crossing points λ. Indeed, the larger the angle θ, the larger the probability that NW segments cross inside the volume. This also clearly appeared in the increase of the number of crossing points going from 362 789 (standard deviation of 806 on 100 runs) for $\theta = 20°$ to 77 200 (standard deviation of 1044 on 100 runs) for $\theta = 25°$. For all values of θ considered, the exponential distribution $1/\lambda \exp(l/\lambda)$ is found to fit very well the data, as in Fig. 3(a) for $\theta = 22.5°$. Moreover, the same homogeneous distribution $1/80$ is obtained for all values of θ for the shortest distance d between two crossing NWs' axes.
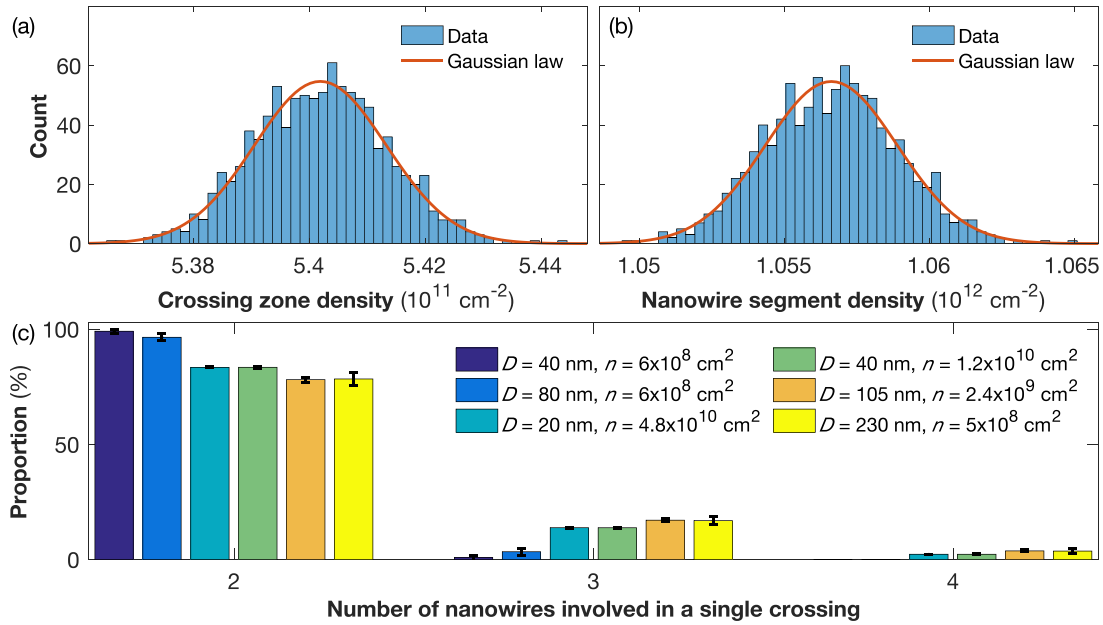
FIG. 4. (a), (b) Count of the (a) crossing zone and (b) nanowire segment densities obtained from 1000 simulations of nanowire networks with $D = 40$ nm, $\theta = 22.5°$, $n = 1.2 \times 10^{10}$ cm^{-2}, and $h = 22$ μm, along with the Gaussian distribution plotted using the mean density and their respective standard deviations (see Table I). (c) Proportion of crossing zones involving two, three, and four nanowires for various network characteristics.

Similar studies have also been performed for the NW networks with various diameters and ion impact surface densities achievable in laboratories, giving very similar results. As an example, Fig. 3(d) shows the exponential distribution of L obtained for a NW network with $D = 105$ nm of diameter, a surface density of impact $n = 2.4 \times 10^9$ cm^{-2}, and a network film thickness $h = 22$ μm, while the angle θ is taken as 22.5°. For these parameters, the impact surface has a side W of 9.1 μm and $N = 1992$ impacts. Here again, the exponential law $1/\lambda \exp(l/\lambda)$ corresponds very well to the data, where a mean value of λ over 1000 runs is 406 nm $\pm$ 3.6 nm. Besides, it is observed that 99% of the segments between two crossing points are below 2 μm. A set of 1000 simulations provides a mean value of about 56 000 crossing points (with standard deviation of about 0.5%) in the volume of interest, which corresponds to about 31 crossing points per μm^3. Here again, 60% of the crossing points involve NWs from perpendicular families. Moreover, as seen in the inset of Fig. 3(d), the shortest distance d between two crossing NWs' axes displays a homogeneous probability density of $1/(2D)$ as obtained for $D = 105$ nm in the inset of Fig. 3(a). The exponential probability density for L and the homogeneous probability density for d remain when changing the value of θ, while only the value of λ is affected. As for the system with 40 nm in diameter, the larger the value of θ, the smaller the value of λ.

One advantageous property of the 3D NW network system is the dense interconnectivity of the NW segments. To describe this characteristic, we investigate the density of NW segments, noted n_{seg}, and the density of crossing zones between the NW segments, noted n_{cross}, for NW networks with various diameters D and impact densities n, while fixing the network thickness h to 22 μm. In contrast to a crossing point that is defined for each pair of NWs that are crossing each other, a crossing zone is defined as a volume where

multiple NWs interconnect, while the NW segments as the segments between crossing zones. Therefore, the density of crossing points is adjusted to accommodate crossing zones involving multiple crossing points (i.e., more than two NWs interconnecting; refer to Supplemental Material [36] Sec. S2 for details). In Figs. 4(a) and 4(b), we show the count histograms for the crossing zone density (a) and NW segment density (b) obtained from 1000 simulations of the system with $D = 40$ nm, $\theta = 22.5°$, $n = 1.2 \times 10^{10}$ cm^{-2}, and $h = 22$ μm. The results are well fitted by Gaussian distributions, plotted using the calculated mean and standard deviation values from the simulations. For the case considered, we obtain $n_{cross} = 5.4 \times 10^{11}$ ($\pm 0.2\%$) and $n_{seg} = 1.1 \times 10^{12}$ ($\pm 0.2\%$). Note that this small standard deviation is anticipated to significantly increase for minor variations in the parameters h, θ, n, or D that can be expected in real NW networks. Table I provides the values for n_{cross} and n_{seg}, as well as the mean distance between two crossing points λ, for the different NW

TABLE I. Mean crossing zone and nanowire segments densities, n_{seg} and n_{cross}, and mean distance between two crossing points λ, obtained over 1000 simulations of nanowire network films with $h = 22$ μm and various combination of NW diameter D and ion impact surface density n.

D (nm)	n (cm^{-2})	n_{cross} (cm^{-2})	n_{seg} (cm^{-2})	λ (nm)
20	4.8×10^{10}	4.3×10^{12}	8.6×10^{12}	109
40	1.2×10^{10}	5.4×10^{11}	1.1×10^{12}	216
105	2.4×10^{9}	5.3×10^{10}	1.0×10^{11}	405
230	5×10^{8}	5.0×10^{9}	9.0×10^{9}	883
40	6×10^{8}	1.6×10^{9}	2.2×10^{9}	2740
80	6×10^{8}	3.1×10^{9}	5.2×10^{9}	1770

networks simulated with h fixed to 22 μm. Similar Gaussian distributions are obtained for all the studied NW networks (see Supplemental Material [36] Sec. S2 for the distributions, as well as the mean and standard deviation values for n_{cross} and n_{seg}). Our simulations with various NW network parameters n and D reveals that the density of crossing points between pairs of NWs varies as $n^2 D$ (see Supplemental Material [36] Sec. S2). This relationship can be attributed to the fact that the number of NWs per cm^2 is directly proportional to n. Assuming that the probability of two NWs to cross is independent of the number of NWs, then the number of crossing points made by each of the n NWs will be proportional to the number n of NWs; i.e., the density of crossing points is proportional to n^2. Additionally, the probability of crossing points is found to be proportional to D, as suggested by the condition for crossing $|d| \leqslant D$. Then, the adjustment made to calculate the density of crossing zones results in a decrease compared to the density of crossing points. This corrective factor is found to be proportional to the network packing factor P (i.e., proportional to nD^2), as an increasing packing factor induces an increasing proportion of crossing zones involving more than two NWs (see Supplemental Material [36] Sec. S3). Importantly, NW networks with $D = 20$ nm and $n = 4.8 \times 10^{10}$ cm^{-2} exhibit up to about 10^{13} interconnected segments per cm^2. This has high interest for neuromorphic computing applications. Indeed, the human brain is estimated to host in the range of 10^{14} synaptic connections [37–42]. Interestingly, 10^{14} interconnections can be achieved with a network of about 10 cm^2. Note that in the real system, the angle θ varies between 20° and 25°, thereby allowing for additional crossings between NWs from the same families. Consequently, the values reported in Table I are expected to be underestimated.

In Fig. 4(c), we present the proportion of crossing zones involving two, three, or four NWs for various networks with given n or D characteristics. As depicted, the proportion of crossing zones involving more than two NWs increases with increasing n or D. Notably, we observe that the proportion of crossing zones involving two NWs is directly dependent on the NW network packing factor (see Supplemental Material [36] Sec. S3 for further details). Note that crossing zones can involve more than four NWs in the systems with $D = 105$ nm and $n = 2.4 \times 10^9$ cm^{-2} and $D = 230$ nm and $n = 5 \times 10^8$ cm^{-2}. However, these crossing zones account for less than 1% of the total crossing zones in the system.

These preliminary results can be used as a base to study physical properties of interest within complex 3D network of NWs with dense interconnectivity, such as electrical or heat transport, magnetism, or temperature distribution—this by simulating various smaller and simpler NW crossing configurations of the system and utilizing the statistical properties derived here to reconstruct the anticipated behavior of the en-

tire system. It should be noticed that 3D NW network systems remain very complex nanostructures and additional imperfections such as defects in the template or inhomogeneous growth can impact the structure.

III. CONCLUSION

In this study, we characterize analytically some geometric properties of three-dimensional interconnected nanowire networks with selected characteristics. We observe an exponential distribution of the nanowire segment size between two interconnections, indicating a very large number of short nanowires. Our investigation reveals that altering the angle θ affects the network's properties. As θ increased, the mean interdistance between two crossing points decreased, aligning with the increased probability of NW segments crossing within the volume. This trend is consistent across varying values of θ, with the exponential distribution fitting the data effectively. Simulations of networks with different nanowire diameters and ion impact surface densities also provide similar results. The densities of crossing zones and interconnected nanowire segments are proportional to $n^2 D$ multiplied by a factor dependent on the nanowire packing factor $P = n\pi D^2 / 4$, where n and D refer to the ion impact surface density and nanowire diameter, respectively. Importantly, these NW networks demonstrate the potential for achieving up to about 10^{13} interconnected segments per cm^2, a crucial factor for applications in neuromorphic computing. Notably, our findings suggest that a network covering approximately 10 cm^2 could achieve the significant 10^{14} synaptic connections estimated in the human brain. To conclude, our analytical study provides valuable insights into the geometric properties and interconnections within three-dimensional nanowire networks. These findings contribute to our understanding of the impact of key parameters on network characteristics and highlight the potential of such networks for applications requiring dense interconnectivity.

[1] M. Rauber, I. Alber, S. Müller, R. Neumann, O. Picht, C. Roth, A. Schökel, M. E. Toimil-Molares, and W. Ensinger, Highly-ordered supportless three-dimensional nanowire networks with tunable complexity and interwire connectivity for device integration, Nano Lett. **11**, 2304 (2011).

[2] J. Martín, M. Martín-González, J. F. Fernández, and O. Caballero-Calero, Ordered three-dimensional interconnected

nanoarchitectures in anodic porous alumina, Nat. Commun. **5**, 5130 (2014).

[3] E. Araujo, A. Encinas, Y. Velázquez-Galván, J. M. Martinez-Huerta, G. Hamoir, E. Ferain, and L. Piraux, Artificially modified magnetic anisotropy in interconnected nanowire networks, Nanoscale **7**, 1485 (2015).

[4] L. Piraux, T. d. C. S. C. Gomes, F. A. Araujo, and J. d. l. T. Medina, 3D magnetic nanowire networks, in *Magnetic Nano- and Microwires*, edited by Manuel Vázquez, 2nd ed. (Elsevier, Sawston, Cambridge, UK, 2020), Chap. 27.

[5] T. d. C. S. C. Gomes, N. Marchal, F. A. Araujo, Y. V. Galván, J. d. l. T. Medina, and L. Piraux, Magneto-transport in flexible 3D networks made of interconnected magnetic nanowires and nanotubes, Nanomaterials **11**, 221 (2021).

[6] W. Wang, M. Tian, A. Abdulagatov, S. M. George, Y.-C. Lee, and R. Yang, Three-dimensional Ni/TiO_2 nanowire network for high areal capacity lithium ion microbattery applications, Nano Lett. **12**, 655 (2012).

[7] C. Wei, H. Pang, B. Zhang, Q. Lu, S. Liang, and F. Gao, Two-dimensional β-MnO_2 nanowire network with enhanced electrochemical capacitance, Sci. Rep. **3**, 2193 (2013).

[8] A. Vlad, V.-A. Antohe, J. M. Martinez-Huerta, E. Ferain, J.-F. Gohy, and L. Piraux, Three-dimensional interconnected Ni_{core}-NiO_{shell} nanowire networks for lithium microbattery architectures, J. Mater. Chem. A **4**, 1603 (2016).

[9] O. S. Kwon, S. J. Park, H. Yoon, and J. Jang, Highly sensitive and selective chemiresistive sensors based on multidimensional polypyrrole nanotubes, Chem. Commun. **48**, 10526 (2012).

[10] L. Piraux, V.-A. Antohe, E. Ferain, and D. Lahem, Self-supported three-dimensionally interconnected polypyrrole nanotubes and nanowires for highly sensitive chemiresistive gas sensing, RSC Adv. **6**, 21808 (2016).

[11] I. Paulowicz, V. Hrkac, S. Kaps, V. Cretu, O. Lupan, T. Braniste, V. Duppel, I. Tiginyanu, L. Kienle, R. Adelung, and Y. K. Mishra, Three-dimensional SnO_2 nanowire networks for multifunctional applications: From high-temperature stretchable ceramics to ultraresponsive sensors, Adv. Electron. Mater. **1**, 1500081 (2015).

[12] M. R. J. Scherer and U. Steiner, Efficient electrochromic devices made from 3D nanotubular gyroid networks, Nano Lett. **13**, 3005 (2013).

[13] E. J. W. Crossland, M. Kamperman, M. Nedelcu, C. Ducati, U. Wiesner, D. M. Smilgies, G. E. S. Toombes, M. A. Hillmyer, S. Ludwigs, U. Steiner, and H. J. Snaith, A bicontinuous double gyroid hybrid solar cell, Nano Lett. **9**, 2807 (2009).

[14] S. Wang, L.-P. Xu, H.-W. Liang, S.-H. Yu, Y. Wen, S. Wang, and X. Zhang, Self-interconnecting Pt nanowire network electrode for electrochemical amperometric biosensor, Nanoscale **7**, 11460 (2015).

[15] S. Rahong, T. Yasui, T. Yanagida, K. Nagashima, M. Kanai, A. Klamchuen, G. Meng, Y. He, F. Zhuge, N. Kaji, T. Kawai, and Y. Baba, Ultrafast and wide range analysis of DNA molecules using rigid network structure of solid nanowires, Sci. Rep. **4**, 5252 (2014).

[16] S. Rahong, T. Yasui, T. Yanagida, K. Nagashima, M. Kanai, G. Meng, Y. He, F. Zhuge, N. Kaji, T. Kawai, and Y. Baba, Three-dimensional nanowire structures for ultra-fast separation of DNA, protein and RNA molecules, Sci. Rep. **5**, 10584 (2015).

[17] C. Liu, C. Wu, Y. Zhao, Z. Chen, T.-L. Ren, Y. Chen, and G. Zhang, Actively and reversibly controlling thermal conductivity in solid materials, Phys. Rep. **1058**, 1 (2024).

[18] E. C. Burks, D. A. Gilbert, P. D. Murray, C. Flores, T. E. Felter, S. Charnvanichborikarn, S. O. Kucheyev, J. D. Colvin, G. Yin, and K. Liu, 3D nanomagnetism in low density interconnected nanowire networks, Nano Lett. **21**, 716 (2021).

[19] T. d. C. S. C. Gomes, J. d. l. T. Medina, Y. G. Velázquez-Galván, J. M. Martínez-Huerta, A. Encinas, and L. Piraux, Interplay between the magnetic and magneto-transport properties of 3D interconnected nanowire networks, J. Appl. Phys. **120**, 043904 (2016).

[20] T. d. C. S. C. Gomes, J. d. l. T. Medina, M. Lemaitre, and L. Piraux, Magnetic and magnetoresistive properties of 3D interconnected NiCo nanowire networks, Nanoscale Res. Lett. **11**, 466 (2016).

[21] A. Fernández-Pacheco, R. Streubel, O. Fruchart, R. Hertel, P. Fischer, and R. P. Cowburn, Three-dimensional nanomagnetism, Nat. Commun. **8**, 15756 (2017).

[22] T. d. C. S. C. Gomes, N. Marchal, F. A. Araujo, and L. Piraux, Tunable magnetoresistance and thermopower in interconnected NiCr and CoCr nanowire networks, Appl. Phys. Lett. **115**, 242402 (2019).

[23] M. F. P. Wagner, A. S. Paulus, J. Brötz, W. Sigle, C. Trautmann, K.-O. Voss, F. Völklein, and M. E. Toimil-Molares, Effects of size reduction on the electrical transport properties of 3D Bi nanowire networks, Adv. Electron. Mater. **7**, 2001069 (2021).

[24] T. d. C. S. C. Gomes, N. Marchal, F. A. Araujo, and L. Piraux, Flexible thermoelectric films based on interconnected magnetic nanowire networks, J. Phys. D: Appl. Phys. **55**, 223001 (2022).

[25] N. Marchal, T. d. C. S. C. Gomes, F. A. Araujo, and L. Piraux, Interplay between diffusion and magnon-drag thermopower in pure iron and dilute iron alloy nanowire networks, Sci. Rep. **13**, 9280 (2023).

[26] L. Piraux, N. Marchal, P. Van Velthem, T. da Câmara Santa Clara Gomes, E. Ferain, J.-P. Issi, and V.-A. Antohe, Polycrystalline bismuth nanowire networks for flexible longitudinal and transverse thermoelectrics, Nanoscale **15**, 13708 (2023).

[27] T. d. C. S. C. Gomes, N. Marchal, F. A. Araujo, and L. Piraux, Flexible active Peltier coolers based on interconnected magnetic nanowire networks, Nanomaterials **13**, 1735 (2023).

[28] T. d. C. S. C. Gomes, F. A. Araujo, and L. Piraux, Making flexible spin caloritronic devices with interconnected nanowire networks, Sci. Adv. **5**, eaav2782 (2019).

[29] F. A. Araujo, T. d. C. S. C. Gomes, and L. Piraux, Magnetic control of flexible thermoelectric devices based on macroscopic 3D interconnected nanowire networks, Adv. Electron. Mater. **5**, 1800819 (2019).

[30] N. Marchal, T. d. C. S. C. Gomes, F. A. Araujo, and L. Piraux, Large spin-dependent thermoelectric effects in NiFe-based interconnected nanowire networks, Nanoscale Res. Lett. **15**, 137 (2020).

[31] T. d. C. S. C. Gomes, N. Marchal, F. A. Araujo, and L. Piraux, Spin caloritronics in 3D interconnected nanowire networks, Nanomaterials **10**, 2092 (2020).

[32] T. d. C. S. C. Gomes, N. Marchal, F. A. Araujo, and L. Piraux, Magnetically activated flexible thermoelectric switches based

on interconnected nanowire networks, Adv. Mater. Technol. **7**, 2101043 (2022).

[33] D. Bhattacharya, Z. Chen, C. J. Jensen, C. Liu, E. C. Burks, D. A. Gilbert, X. Zhang, G. Yin, and K. Liu, 3D interconnected magnetic nanowire networks as potential integrated multistate memristors, Nano Lett. **22**, 10010 (2022).

[34] G. Milano, G. Pedretti, K. Montano, S. Ricci, S. Hashemkhani, L. Boarino, D. Ielmini, and C. Ricciardi, *In materia* reservoir computing with a fully memristive architecture based on self-organizing nanowire networks, Nat. Mater. **21**, 195 (2022).

[35] C. Chopin, S. de Wergifosse, N. Marchal, P. Van Velthem, L. Piraux, and F. A. Araujo, Memristive and tunneling effects in 3D interconnected silver nanowires, ACS Omega **8**, 6663 (2023).

[36] See Supplemental Material at http://link.aps.org/supplemental/10.1103/PhysRevResearch.6.023211 for additional details on the computation of nanowire segment length distribution, the statistical distributions of the densities of crossing zones and interconnected nanowire segments, and the proportion of crossing zones with a given number of nanowires.

[37] G. M. Shepherd, *The Synaptic Organization of the Brain* (Oxford University Press, New York, 1998).

[38] C. Koch, *Biophysics of Computation: Information Processing in Single Neurons* (Oxford University Press, New York, 1999).

[39] D. A. Drachman, Do we have brain to spare? Neurology **64**, 2004 (2005).

[40] J. L. Saver, Time is brain-quantified, Stroke **37**, 263 (2006).

[41] F. A. C. Azevedo, L. R. B. Carvalho, L. T. Grinberg, J. M. Farfel, R. E. L. Ferretti, R. E. P. Leite, W. J. Filho, R. Lent, and S. Herculano-Houzel, Equal numbers of neuronal and non-neuronal cells make the human brain an isometrically scaled-up primate brain, J. Comp. Neurol. **513**, 532 (2009).

[42] A. Motta, M. Berning, K. M. Boergens, B. Staffler, M. Beining, S. Loomba, P. Hennig, H. Wissler, and M. Helmstaedter, Dense connectomic reconstruction in layer 4 of the somatosensory cortex, Science **366**, eaay3134 (2019).